

Guidestar-Free Adaptive Optics with Asymmetric Apertures

Weiyun Jiang*
 wyjiang@rice.edu
 Rice University
 Houston, Texas, USA

Christopher A. Metzler†
 metzler@umd.edu
 University of Maryland College Park
 College Park, MD, USA

Haiyun Guo*
 hg39@rice.edu
 Rice University
 Houston, Texas, USA

Ashok Veeraraghavan†
 vashok@rice.edu
 Rice University
 Houston, Texas, USA

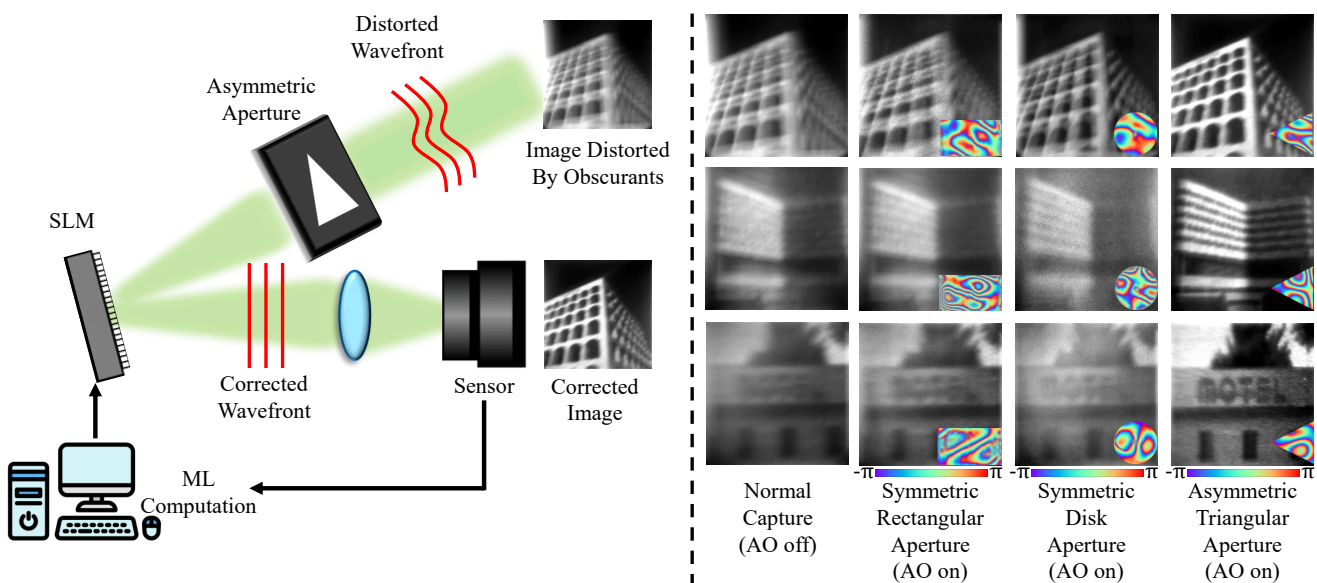


Figure 1: Guidestar-free adaptive optics with asymmetric apertures. Our system combines asymmetric apertures with machine learning to image through severe optical aberrations without wavefront sensors or guidestars. By contrast, conventional symmetric apertures suffer from a conjugate-flip ambiguity, which makes computational wavefront sensing—and by extension AO—ineffective. The above results were experimentally captured with a tabletop prototype.

Abstract

This work introduces the first closed-loop adaptive optics (AO) system capable of optically correcting aberrations in real-time without a guidestar or a wavefront sensor. Nearly 40 years ago, Cederquist et al. demonstrated that asymmetric apertures enable phase retrieval (PR) algorithms to perform fully computational wavefront sensing, albeit at a high computational cost. More recently, Chimitt et al. extended this approach with machine learning and demonstrated real-time wavefront sensing using only a single (guidestar-based) point-spread-function (PSF) measurement. Inspired by these works, we introduce a *guidestar-free* AO framework built around asymmetric apertures and machine learning. Our approach combines three key elements: (1) an asymmetric aperture placed in the optical path that enables PR-based wavefront sensing, (2) a pair of machine learning algorithms that estimate the PSF from natural scene measurements and reconstruct phase aberrations, and (3) a

spatial light modulator that performs optical correction. We experimentally validate this framework on dense natural scenes imaged through unknown obscurants. Our method outperforms state-of-the-art guidestar-free wavefront shaping methods, using an order of magnitude fewer measurements and three orders of magnitude less computation.

Keywords

Guidestar-free, Imaging through obscurants, Asymmetric apertures, Wavefront shaping, Adaptive optics

1 Introduction

Optical imaging systems often suffer from wavefront distortions caused by obscurants, including atmospheric turbulence [5, 8, 23, 47], biological tissues [2, 3, 30], fog [19, 22, 41], rain [16], and imperfect lenses [10, 26, 40]. These obscurants scatter and distort light, producing blurry images and severely reducing visibility [39].

*Both authors contributed equally to this work.

†Both authors contributed equally to this work.

Adaptive optics (AO) is a powerful tool for imaging through obscurants, which works by actively measuring and correcting wavefront distortions. AO enables high-quality imaging in fields such as astronomy [37, 38], biomedical microscopy [1, 34, 51], communications [44, 45], and surveillance [4, 46]. However, existing AO methods require additional specialized hardware [7, 31, 36, 50] or rely on multiple coded measurements [14, 17, 21, 29, 33, 48, 49].

Is it possible to build an AO system without any additional hardware or measurements, using only computation? An optical system’s point-spread-function (PSF) is related to its wavefront error through a Fourier magnitude squared relationship. In principle, one could directly estimate a system’s wavefront error from its PSF by solving a phase retrieval (PR) problem. Unfortunately, for most optical systems, this problem is fundamentally ill-posed; multiple phase distributions can produce identical intensity patterns due to reflection and conjugation symmetries in the Fourier domain [15, 17]. Cederquist et al. demonstrated that one can remove this ambiguity, and make the PR problem well-posed, by using an asymmetric aperture, which has no conjugate symmetries [6, 27]. See Fig. 2. Still, the high computational costs of iterative phase retrieval algorithms have made computational wavefront sensing systems impractical, until recently.

Chimitt et al. [11, 12] recently introduced a practical fully computational approach to wavefront sensing. Specifically, they showed that with the help of an asymmetric aperture, one can use a computationally efficient neural network to learn a direct mapping from the PSFs to the underlying phase aberrations. However, while their approach eliminates the need for iterative PR, it still requires guidestar-based calibration, where a known point source is used to obtain the PSF before estimating the phase. This reliance on calibrated illumination limits its applicability in uncontrolled environments, where point-source references are generally unavailable.

In this paper, we introduce and experimentally validate a novel guidestar-free adaptive optics framework (Fig. 1). We build on the work of Chimitt et al. [12], reformulating wavefront correction as a PR problem with an asymmetric aperture. However, rather than relying on a guidestar to measure the PSF, our method estimates the PSF from the natural scene measurement using a neural network. This approach eliminates the need for a calibration source and enables practical deployment in real-world imaging scenarios. With the PSF estimate in hand, we use a second neural network to reconstruct the aberration’s phase error. The conjugate of the recovered phase error is then added to the pattern displayed on a spatial light modulator (SLM) to perform optical correction. Unlike existing methods that require guidestars [25], multiple coded measurements [14, 48], or specialized wavefront sensors [7], our approach achieves high-quality imaging through unknown obscurants in a closed loop—it recursively removes residual aberrations and can fully correct severe aberrations in 2–4 iterations—with minimal computational overhead.

Our specific contributions include:

- We propose a novel guidestar-free adaptive optics framework that leverages asymmetric apertures to perform high-quality imaging through obscurants.
- We compare our method against existing state-of-the-art guidestar-free wavefront shaping and image deblurring methods; our method consistently outperforms them while

using an order of magnitude fewer measurements and three orders of magnitude less computation.

- We experimentally validate our method on natural scenes by imaging through various real obscurants, including nail polish, onion skin, and optical diffusers.

2 Related Work

Imaging Through Obscurants. Imaging through obscurants is a persistent challenge in many applications, including astronomy, biomedical microscopy, and surveillance. Conventional AO approaches often rely on specialized wavefront sensors, such as SHWSs [35] and interferometers, to obtain direct measurements of phase distortions. SHWSs utilize arrays of microlenses to focus incident wavefronts onto a detector array, enabling measurement of local wavefront tilts for reconstruction of the entire wavefront. Interferometers [9] assess wavefront aberrations by generating interference patterns between a reference beam and a test beam, facilitating correction through elements such as deformable mirrors (DMs) or spatial light modulators (SLMs). Despite their effectiveness, these methods require dedicated hardware and precise point-source calibration, which restricts their practicality in uncontrolled environments.

To overcome these limitations, recent developments in AO focus on computational techniques that estimate wavefront distortions directly from camera sensor measurements, thus removing the need for guidestars. Phase-diversity based wavefront shaping [14, 48] applies known phase modulations to acquire multiple intensity images and jointly optimizes for both phase aberrations and the target image. Image-guided wavefront shaping [21, 49] begins with a raw, uncorrected measurement and iteratively updates the SLM pattern to enhance image contrast and sharpness. Although these computational methods reduce reliance on specialized sensors and guidestars, they still depend on computationally intensive iterative optimization, which limits their suitability for rapid aberration correction.

In contrast to these works, our method eliminates iterative optimization by employing direct, feedforward neural networks for wavefront correction. Our approach enables significantly faster and more scalable processing, eliminating the need for dedicated wavefront sensors. It directly estimates wavefront corrections from conventional camera sensor measurements, thereby enhancing adaptability for real-world imaging tasks.

Wavefront Sensing with Asymmetric Apertures. Traditional wavefront sensing methods suffer from ambiguities due to symmetric apertures, leading to multiple indistinguishable solutions. To address this, researchers have introduced asymmetric apertures to break these ambiguities. Almost 40 years ago, Cederquist et al. [6] first demonstrated that asymmetric apertures enable PR via iterative optimization, albeit at a high computational cost. Martinache [27] later proposed the Asymmetric Pupil Fourier Wavefront Sensor (APF-WFS), which uses a linear model to estimate phase directly under small aberrations, thereby avoiding iterative retrieval. However, this method requires the assumption that phase aberrations remain within the small-angle approximation, limiting its applicability in real scenarios with larger wavefront distortions. More recently, Chimitt et al. proposed [11] and demonstrated [12] a deep

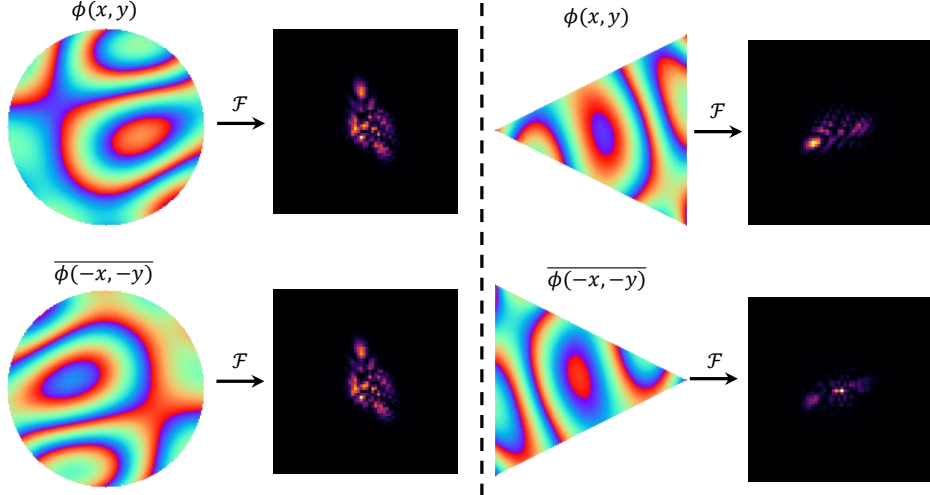


Figure 2: Breaking symmetry with asymmetric triangular apertures enables unique phase retrieval from PSFs. For a circular aperture, the original phase $\phi(x, y)$ and its conjugate-flipped counterpart $\overline{\phi(-x, -y)}$ produce identical PSFs after the Fourier transform, leading to phase ambiguity in intensity-only measurements. In contrast, for a triangular aperture—representative of a broader class of asymmetric apertures such as polygons with an odd number of sides—the wavefront phases $\phi(x, y)$ and $\overline{\phi(-x, -y)}$ yield distinct PSFs. This asymmetry enables unique phase retrieval from intensity measurements, resolving the ambiguity present in symmetric apertures.

learning-based method that combines an asymmetric pupil with a neural network for fast wavefront estimation, learning a direct mapping from the PSF to the phase aberration. Unlike APF-WFS, this approach imposes no strict assumptions on the magnitude of phase aberrations, making it more adaptable to real-world conditions. While these methods improve PR, they rely on direct point-source references (guidestars), limiting their applicability in uncontrolled natural environments. In contrast, our method eliminates the need for the point-source calibration, allowing fully passive wavefront sensing in uncontrolled environments.

3 Imaging Through Obscurants

3.1 Forward Model

In this paper, we assume we are dealing with a spatially invariant forward model, i.e., isoplanatic turbulence or scattering restricted to the memory effect region. Under this model, the measurement process can be described by

$$Y = X \circledast H + \epsilon, \quad (1)$$

where Y denotes the captured sensor measurement, \circledast denotes two-dimensional convolution, X denotes the unknown target scene, H denotes the system's aberrated PSF, and ϵ accounts for additive noise.

We further assume we are dealing with monochromatic and incoherent illumination, such that the system's PSF is described by

$$H = \left| \mathcal{F}\{A \circ e^{j\phi_o}\} \right|^2, \quad (2)$$

where \mathcal{F} denotes the 2D Fourier transform, \circ denotes element-wise multiplication, A denotes the known aperture shape, and ϕ_o denotes the unknown phase aberration/wavefront error [18].

The goal of adaptive optics is to estimate and compensate for the phase aberration ϕ_o . If one were to know ϕ_o , one could place the conjugate phase $-\phi_o$ on an SLM or deformable mirror array at the pupil plane and optically correct for the aberration:

$$Y_{corrected} = X \circledast \left| \mathcal{F}\{A \circ e^{j(\phi_o - \phi_o)}\} \right|^2 + \epsilon = X \circledast H_{corr} + \epsilon, \quad (3)$$

where $H_{corr} = |\mathcal{F}\{A\}|^2$ is a Dirac-like diffraction-limited PSF.

3.2 Closed-Loop Adaptive Optics

Now imagine that, either due to errors in the wavefront estimate or changes in the optical aberration over time, one projects an SLM pattern $\phi_{SLM} \neq -\phi_o$ on the SLM. In this context, an AO system would capture only partially corrected measurements

$$Y_{partial} = X \circledast \left| \mathcal{F}\{A \circ e^{j\phi}\} \right|^2 + \epsilon, \text{ with } \phi = \phi_o + \phi_{SLM}, \quad (4)$$

where ϕ is the residual, partially-compensated wavefront error in the system.

In a closed-loop adaptive optics system, one adaptively compensates for this residual wavefront error. That is, one forms an estimate, $\hat{\phi}$, and then adds its conjugate to the pattern displayed on the SLM: $\phi_{SLM}^{new} = \phi_{SLM}^{old} - \hat{\phi}$. In this work, we develop a closed-loop AO system.

3.3 Wavefront Sensing as Phase Retrieval

Before one can compensate for wavefront errors (residual or not), one first needs to estimate them. While this is typically done using a wavefront sensor, it can also be performed by modeling (2) as a Fourier phase retrieval problem: With a measurement of the PSF H and knowledge of the aperture A in hand, one can solve a phase retrieval problem to reconstruct the wavefront error ϕ .

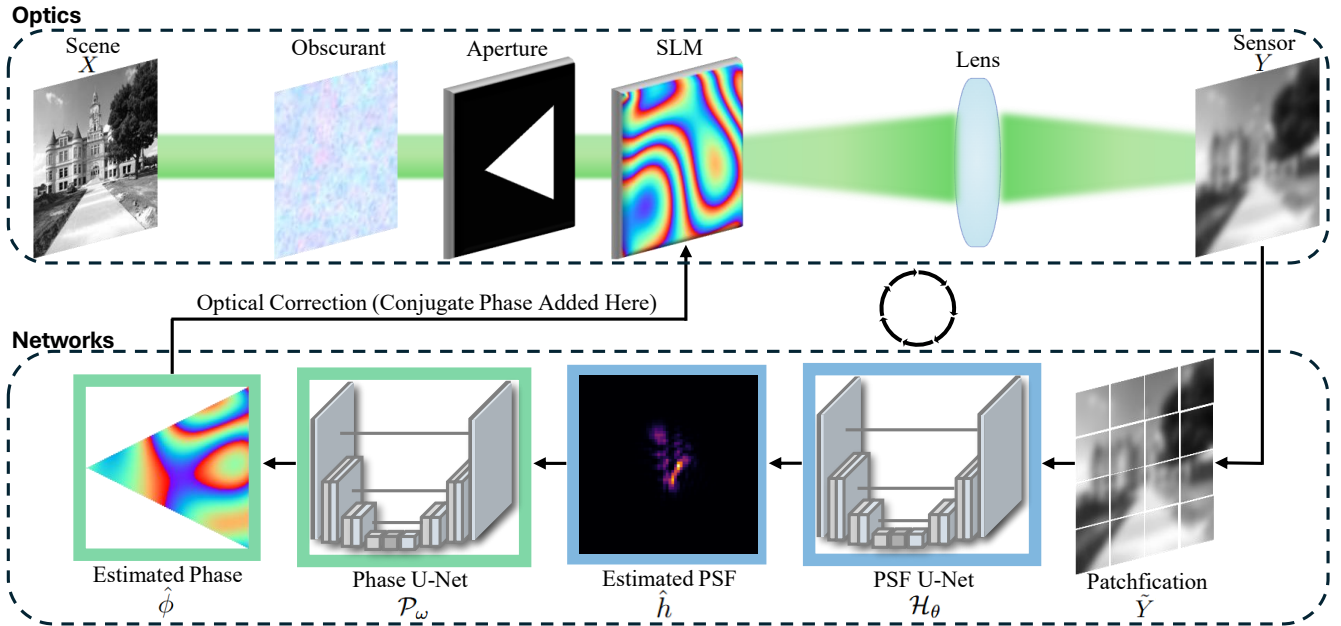


Figure 3: Overview of proposed closed-loop guidestar-free AO system. Light from the scene passes through an obscurant (e.g., nail polish, onion skin, optical diffusers) which introduces an unknown wavefront error ϕ_o . This aberrated wavefront passes through an asymmetric aperture* before reaching a spatial light modulator (SLM) that introduces a phase delay ϕ_{SLM} . A lens forms a blurry and distorted image of the scene, the effective/residual wavefront error of this blurry scene is $\phi = \phi_o + \phi_{SLM}$. The PSF U-Net estimates the PSF from the captured image and the Phase U-Net then forms a prediction, $\hat{\phi}$, of the phase error. We add the conjugate of the estimated phase error ($-\hat{\phi}$) to the SLM optically correct the residual aberration. We repeat the process iteratively until the sensor image is sharp. The results in this manuscript were captured with three AO loops (4 measurements).

*To realize an asymmetric aperture, we display a checkerboard pattern on a phase-only SLM at the regions where we desire zero amplitude [28].

Note, however, that with symmetric apertures, this problem is fundamentally ill-posed because

$$|\mathcal{F}(A_{symm} \circ e^{j\phi})|^2 = |\mathcal{F}(A_{symm} \circ e^{-j\phi_{flip}})|^2,$$

where $e^{-j\phi_{flip}}$ is the conjugated and flipped version of $e^{j\phi}$. The system is non-injective and two completely different wavefront errors—which call for completely different optical correction—produce identical measurements.

Fortunately, asymmetric aperture removes this ambiguity and enables PR based wavefront sensing. See [12] for more information. Fig. 2 illustrates the important role asymmetric apertures play in enabling PR-based wavefront sensing.

4 Guidestar-Free AO Framework

We combine asymmetric apertures and machine learning to create a powerful closed-loop guidestar-free AO system. Our pipeline, illustrated in Fig. 3, images a target scene X through an unknown obscurant. The incoming light is modulated at the pupil plane by an SLM before being imaged onto a camera, which captures a distorted measurement Y . (See Sec. 5.2 for a detailed description of the optical setup.)

Given measurements of this form, our AO system operates in three stages. In the PSF estimation stage, the (isoplanatically) distorted image Y is broken into patches, which are stacked together as multiple channels and processed by the **PSF U-Net** \mathcal{H}_θ , which

estimates the system’s PSF. (Note that this PSF is a function of both the unknown wavefront error ϕ_o and the correction pattern ϕ_{SLM} currently displayed on the SLM.) Next, in the phase error estimation stage, the estimated PSF is passed to the **Phase U-Net** \mathcal{P}_ω , which predicts the associated (residual) wavefront errors. Finally, in the optical correction stage, the conjugate of the wavefront estimate $\hat{\phi}$ is added to the SLM to perform optical correction, and a new image is captured. This three-stage process is repeated until the sensor captures a sharp image or for a fixed number of iterations. For simplicity, all experiments in this manuscript were performed with 3 AO loops (4 measurements total).

Details about each stage of our pipeline are provided below.

4.1 Network Structure

PSF U-Net \mathcal{H}_θ estimates the PSF from the sensor measurements. Given the original sensor measurement $Y \in \mathbb{R}^{1 \times H \times W}$, we first partition it into patches $\tilde{Y} \in \mathbb{R}^{P \times M \times N}$, where P is the number of patches, and M and N denote the spatial dimensions of each patch. The network then processes these patches and outputs an estimated PSF $\hat{h} \in \mathbb{R}^{1 \times M \times N}$.

The PSF U-Net \mathcal{H}_θ , parameterized by θ , follows a 5-layer encoder-decoder architecture with an initial feature size of 128 and a maximum channel capacity of 4096. We stack image patches into multiple channels (rather than feeding in a high-resolution image) to encourage the network to focus on the central region of the PSF, as

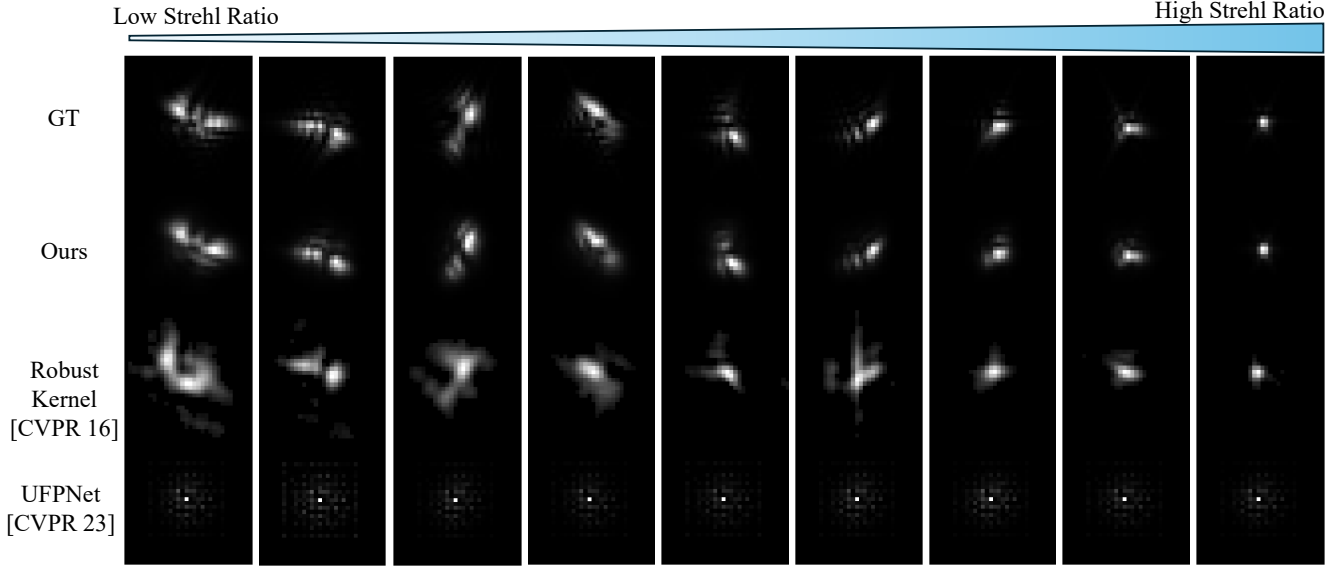


Figure 4: Estimated and ground-truth PSFs. Each column presents a PSF example, arranged in order of increasing Strehl ratio from left to right. The top row shows the ground-truth PSFs, followed by estimates from our method, Robust Kernel [32], and UFPNet [13]. We use the official open-source implementation of UFPNet and the released code of Robust Kernel. Robust Kernel and UFPNet provide sub-optimal kernel estimates because they are designed primarily for image deblurring.

the outer regions contain little meaningful information for phase recovery.

Phase U-Net \mathcal{P}_ω reconstructs the phase aberration from the estimated PSF. Given an estimated PSF $\hat{h} \in \mathbb{R}^{1 \times M \times N}$, we first apply zero-padding to expand it to $\tilde{h} \in \mathbb{R}^{1 \times H \times W}$, matching the full sensor resolution. The network then processes the padded PSF and predicts the corresponding phase aberration $\hat{\phi} \in \mathbb{R}^{1 \times H \times W}$.

The Phase U-Net \mathcal{P}_ω , parameterized by ω , adopts a 5-layer encoder-decoder structure with an initial feature size of 32 and a maximum channel capacity of 512. Unlike the PSF U-Net, this network requires significantly fewer feature channels since asymmetric apertures break the phase retrieval ambiguity, making phase reconstruction a well-conditioned problem.

4.2 Two-Step Network Optimization

We optimize our network in two steps to ensure stable convergence and effective learning of both PSF estimation and phase reconstruction. While the pipeline performs iterative correction during inference, the training procedure for both networks is strictly feed-forward, with no feedback or iterative updates between iterations. Each training sample is processed by the networks in a single forward pass, without any iterative refinement. Iterative correction is applied only at inference time, not during training.

Step 1: Independent Training. In the first independent training step, we train the PSF U-Net \mathcal{H}_θ and the Phase U-Net \mathcal{P}_ω separately. The PSF U-Net is optimized using an L_2 loss to minimize the reconstruction error between the predicted and ground truth PSFs, following:

$$\min_\theta \|\mathcal{H}_\theta(\tilde{Y}) - h_{gt}\|_2^2, \quad (5)$$

where h_{gt} is the ground truth PSF.

Meanwhile, the Phase U-Net \mathcal{P}_ω is trained using a gradient-based loss to enforce smoothness and preserve local variations in the reconstructed phase. Since absolute phase values may shift arbitrarily (e.g., adding a constant to all phase values does not affect the physical wavefront), we minimize the discrepancy between the phase gradients rather than absolute values:

$$\min_\omega \left\| \nabla_x \mathcal{P}_\omega(\tilde{h}) - \nabla_x \phi_{gt} \right\|^2 + \left\| \nabla_y \mathcal{P}_\omega(\tilde{h}) - \nabla_y \phi_{gt} \right\|^2, \quad (6)$$

where ∇_x and ∇_y represent horizontal and vertical gradient respectively, and ϕ_{gt} denotes ground truth phase.

Step 2: Joint Optimization. In the second joint optimization step, we fine-tune the entire network by training the Phase U-Net \mathcal{P}_ω while keeping the PSF U-Net \mathcal{H}_θ fixed. By freezing \mathcal{H}_θ , we ensure that the learned PSF estimation remains stable while allowing \mathcal{P}_ω to refine phase predictions based on more stable PSF inputs. This step improves the consistency between PSF estimation and phase reconstruction. We continue optimizing \mathcal{P}_ω using the same gradient-based loss (Eq. 6).

4.3 Training & Datasets

Networks were trained using entirely simulated data. All training and experiments in this work are implemented in PyTorch and conducted on a single NVIDIA A100 GPU. Although our proposed pipeline operates iteratively during inference (see Fig. 3), the network is trained in a feedforward manner using two-step optimization, as described in Sec. 4.2.

The training procedure consists of two steps. In the first step, the Phase U-Net and PSF U-Net are optimized separately. To train the



Figure 5: Simulated results for guidestar-free wavefront shaping compared with NeuWS. This figure presents a qualitative comparison between our method and the state-of-the-art guidestar-free wavefront shaping method, NeuWS [14]. Each column represents a different method/measurement setting. NeuWS includes both digital and optical reconstruction results, while our method and our method combined with Chimitt et al. [12] provide only optical correction results. Notably, our approach achieves high-quality image restoration with only four measurements, whereas the performance of NeuWS declines significantly as the number of measurements decreases from 16 to 4. These results demonstrate that our method enables high-quality optical reconstruction using only four measurements, substantially reducing the measurement requirements compared to NeuWS.

PSF U-Net, we use 100,000 images from the MIT Places2 dataset [52] and a total of 7.8 million PSFs. During training, we randomly sample an image and a PSF to generate blurred image-PSF pairs as input. Each image is resized to 256×256 and divided into sixteen 64×64 patches. To train the Phase U-Net, we generate a paired phase-PSF dataset by simulating random phase aberrations using the first six orders of Zernike polynomials. The corresponding PSFs are computed by taking the squared magnitude of the Fourier transform of the complex pupil function, where the pupil function is defined by the chosen aperture and the simulated phase aberrations, following Eqn. 2. Both networks are trained for 100 epochs with a batch size of 256.

In the second step, we freeze the weights of the PSF U-Net and fine-tune the Phase U-Net, which takes as input the estimated PSF produced by the frozen PSF U-Net.

4.4 Inference

During the experiments, we perform 3 adaptive optics loops (4 measurements total). Most optical aberrations are corrected in the first two loops, with subsequent loops further reducing residual errors.

5 Results

We evaluate the proposed method in two main aspects: the accuracy of PSF estimation in simulation, and the effectiveness of wavefront shaping in both simulated environments and real-world imaging through obscurants.

Table 1: Quantitative comparison of PSF estimation accuracy. The proposed method quantitatively outperforms Robust Kernel [32] and UFPNet [13] in terms of PSNR and SSIM. Robust Kernel and UFPNet provides sub-optimal kernel estimates because they are designed primarily for image deblurring.

Method	PSNR	SSIM
Ours	39.22	0.9891
Robust Kernel [CVPR 2016]	24.42	0.8960
UFPNet [CVPR 2023]	17.23	0.6359

5.1 Simulated Results

5.1.1 Accuracy of PSF Estimation. To evaluate the accuracy of our estimated PSFs, we construct a hold-out test set consisting of 3,000 images from the MIT Places2 [52] dataset and 3,000 previously unseen PSFs generated using Zernike polynomials. The test blurred images are synthesized by convolving the clean test images with these PSFs. We use these blurred images to evaluate the accuracy of PSF estimation of our proposed PSF U-Net. For comparison, we include the following baseline methods:

- **Robust Kernel** [32]: A non-deep-learning blind deblurring method that removes outliers (such as saturation and non-Gaussian noise) from salient edge selection to enable accurate kernel estimation and restoration.
- **UFPNet** [13]: A deep learning-based image deblurring method that incorporates non-uniform kernel estimation via normalizing flow-based motion priors and uncertainty learning.

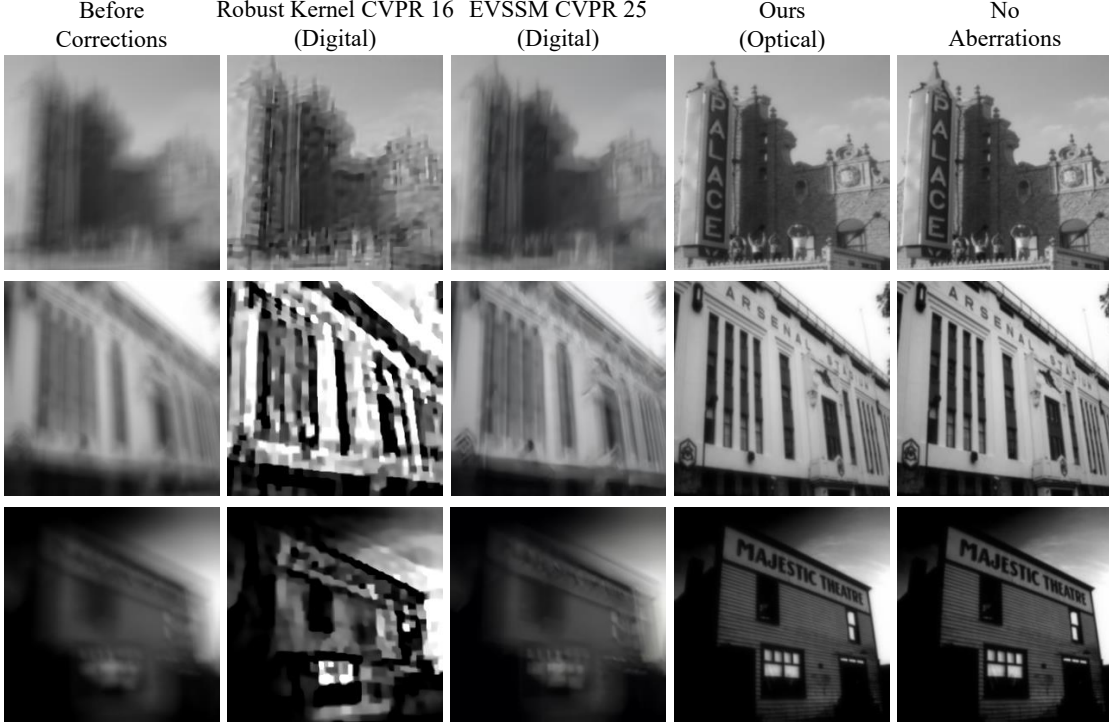


Figure 6: Simulated comparisons against deblurring baselines. This figure compares the performance of Robust Kernel [32], a non-deep learning image deblurring method, EVSSM [24], a state-of-the-art deep learning-based deblurring method, and our proposed approach, which implements optical correction. Each row presents a different scene, and each column displays results from a specific method, including cases before correction and those with no aberrations as references. While both Robust Kernel and EVSSM produce digital corrections, our method performs optical correction and is able to restore image quality in cases where image deblurring algorithms fail.

Table 2: Quantitative evaluation of existing SOTA image deblurring and guidestar-free wavefront shaping methods on both simulated and real experiments. We report PSNR/SSIM for image quality, execution time, and computational cost (FLOPs). Our method achieves significantly higher image quality with minimal computation, outperforming both digital and optical baselines. **Bold** indicates the best result, and underline indicates the second-best result for each column.

Methods	Correction Types	Simulation		Real		Computation Cost	
		PSNR	SSIM	PSNR	SSIM	Time (sec)	FLOPs (G)
Robust Kernel	Digital	15.61	0.4062	14.75	0.2558	~90	~2
EVSSM	Digital	18.53	0.5027	<u>15.38</u>	<u>0.2723</u>	<u>~0.1</u>	~150
NeuWS 4 meas.	Digital	15.33	0.3965	-	-	~15	~4.4e3
	Optical	14.69	0.3912	-	-		
NeuWS 16 meas.	Digital	20.97	0.6208	-	-	~20	~1.66e4
	Optical	23.47	0.7277	-	-		
WaveMo + NeuWS 16 meas.	Digital	21.13	0.6585	-	-	~20	~1.7e4
	Optical	27.47	0.8516	-	-		
NeuWS 100 meas.	Digital	25.58	0.8219	-	-	~85	~1e5
	Optical	39.23	0.9877	-	-		
Ours + Chimitt et al.	Optical	35.34	0.9671	-	-	~0.05	<u>~16</u>
Ours	Optical	37.95	<u>0.9865</u>	25.33	0.7421	~0.05	<u>~16</u>

Note that to date, kernel estimation methods have been primarily designed to enable image deblurring; therefore, their kernel estimation performance may be suboptimal when directly evaluated for PSF recovery.

In Fig. 4, our method produces PSF estimates that are visually closest to the ground truth. Table 1 reports the PSNR and SSIM of the estimated PSFs for our method, Robust Kernel, and UFPNet, providing a quantitative comparison of estimation accuracy.

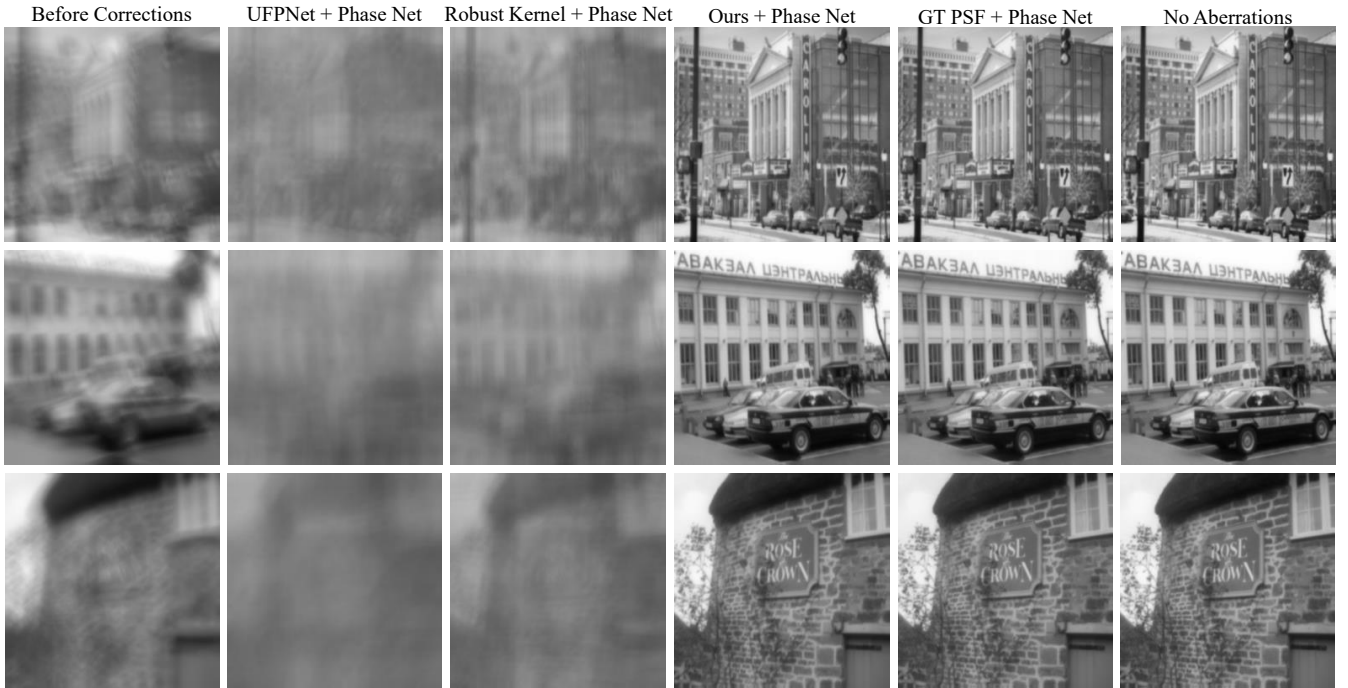


Figure 7: Ablation on PSF estimation. This figure evaluates the effect of different PSF estimation methods on wavefront correction performance. We compare reconstructions using PSFs estimated by UFPNet [13] and Robust Kernel [32] with those obtained from our method, as well as from the ground-truth PSF. Our estimated PSF enables effective correction and produces results comparable to those achieved with the ground-truth PSF, while using PSFs estimated by UFPNet or Robust Kernel does not yield satisfactory restoration.

Table 3: Wavefront shaping performance with different PSF estimation methods. PSNR and SSIM values for reconstructions using various PSF estimation approaches. Our method (Ours + Phase Net) achieves performance that is comparable to using the ground-truth PSF, while UFPNet and Robust Kernel provide only limited correction.

Methods	PSNR	SSIM
UFPNet + Phase Net	15.65	0.3549
Robust Kernel + Phase Net	16.85	0.3954
Ours + Phase Net	38.89	0.9884
GT + Phase Net	40.90	0.9961

5.1.2 Wavefront Shaping Reconstructions. To evaluate the wavefront shaping performance of our proposed method, we use a separate hold-out test set comprising 3,000 images from the MIT Places2 dataset and 3,000 unseen PSFs generated using Zernike polynomials. The test blurred images are synthesized by convolving the clean test images with these PSFs. Our evaluation follows a three-stage pipeline: (1) estimate the PSF from the blurred images using the proposed PSF U-Net, (2) estimate the associated wavefront error, and (3) perform optical correction by adding the conjugate of the estimated wavefront error. We compare our approach with both state-of-the-art wavefront shaping methods and image deblurring methods. The wavefront shaping baselines are as follows:

- **NeuWS** [14]: A guidestar-free wavefront shaping method that jointly estimates the wavefront error and the clean image by applying random phase modulations and acquiring multiple modulated measurements.

NeuWS employs a spatial light modulator (SLM) in the optical path to apply random phase masks across different measurements. Each mask produces a distinct modulated measurement of the same scene. The algorithm alternates between recovering the underlying object and estimating the aberrated wavefront from this set of measurements. In our implementation, we follow the procedure described in the original paper and generate synthetic measurements using Zernike polynomials. For each scene, we sample random phase modulations, apply them to the wavefront, and propagate the result to the sensor plane to form modulated intensity images. These simulated sensor images, together with the applied phase modulations, are then provided as inputs to the iterative reconstruction algorithm of NeuWS.

- **WaveMo** [48]: A guidestar-free method that extends NeuWS by replacing random phase modulation with learned phase modulation strategies.

Instead of selecting the modulations independently at random, WaveMo employs a trained modulation generator network that produces phase masks optimized for the intensity measurements. This improves measurement efficiency and substantially reduces the number of required measurements. In our implementation, we apply the learned modulation

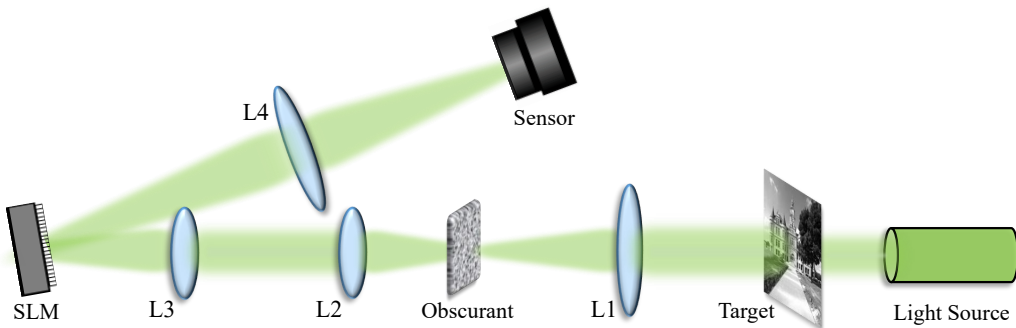


Figure 8: Optical setup. A spatially incoherent light source illuminates the target and passes through the obscurant. The SLM is positioned at the Fourier plane to project the estimated phase patterns. The corrected wavefront is then imaged onto a camera.

patterns released with the original work to the input wavefront and propagate them to the sensor plane to generate the measurements. These measurements, together with the corresponding learned modulation patterns, are then provided as inputs to the iterative reconstruction algorithm of NeuWS.

- **Chimitt et al. [12]:** A guidestar-based method that estimates the Zernike coefficients of the wavefront error. Chimitt et al. propose a guidestar-based wavefront correction framework that assumes access to a bright point-source guidestar propagating through the same obscurant as the target object. The recorded PSF of the guidestar is used to estimate Zernike coefficients of the wavefront error, which then drive a correction device (e.g., deformable mirror or SLM) to restore image quality. This approach is highly effective when a guidestar is available, but is not applicable in general guidestar-free scenarios.

To enable comparison under guidestar-free conditions, we adapt Chimitt et al.’s method by replacing the explicit guidestar PSF measurement with the PSF predicted by our PSF U-Net from a blurred intensity measurement. In this hybrid variant, the Zernike coefficient regression of Chimitt et al. remains unchanged; however, its input PSF comes from our network’s estimation rather than the ground-truth guidestar PSF assumed in their work. This adaptation allows us to compare our framework against a strong guidestar-based baseline while ensuring consistent evaluation settings (i.e., no actual guidestar present).

In guidestar-free wavefront shaping, the number of measurements corresponds to the number of distinct phase-modulated sensor images captured. Each measurement is obtained by applying a different modulation pattern and recording the resulting intensity image at the detector. More measurements provide richer diversity for wavefront estimation, but at the cost of increased computation and acquisition time.

As shown in Table 2, NeuWS requires nearly 100 measurements to achieve satisfactory reconstruction quality, and also incurs a high computational cost. With fewer measurements, its performance degrades substantially—at around 16 measurements it produces only reasonable reconstructions, and with 4 measurements the results degrade significantly. These trends are also evident qualitatively in

Fig. 5, where NeuWS reconstructions worsen visibly as the number of measurements decreases. In contrast, our method achieves high-quality reconstruction with only four measurements, while requiring orders of magnitude fewer computations and significantly shorter runtime. The compared image deblurring methods include:

- **EVSSM [24]:** An efficient state space model designed for image deblurring.
- **Robust Kernel [32]:** A classical deblurring method that performs iterative kernel estimation and multi-scale deconvolution.

As shown in Fig. 6, both Robust Kernel and EVSSM fail to restore images degraded by strong aberrations. Robust Kernel, a classical iterative deblurring method, leaves heavy artifacts and recovers little fine structure, while EVSSM, despite being a state-of-the-art deep learning model for image deblurring, also struggles and produces results with severe residual blur. In contrast, our proposed method, which performs optical correction, restores images that closely resemble the no-aberration reference. These results highlight that conventional image deblurring approaches, whether classical or learning-based, are not effective for imaging through complex aberrations, whereas our wavefront correction framework successfully recovers high-quality images.

5.1.3 Ablation on PSF Estimation. To investigate the impact of different PSF estimation methods on wavefront correction, we conduct an ablation study comparing several approaches. Fig. 7 shows qualitative results for three representative test scenes. For each scene, we present reconstructions obtained by applying wavefront correction using PSFs estimated by UFPNet [13], Robust Kernel [32], our proposed method, and the ground-truth PSF. We also include the original uncorrected image and a reference image without aberrations.

The results indicate that using PSFs estimated by either UFPNet or Robust Kernel does not yield satisfactory wavefront correction. The restored images remain blurry and exhibit little improvement over the uncorrected input. In contrast, our estimated PSFs enable effective correction and produce reconstructions that are visually comparable to those achieved with the ground-truth PSF. This demonstrates that accurate PSF estimation is critical for successful wavefront correction and highlights the advantage of our proposed method over prior approaches that primarily focus on image deblurring rather than precise PSF recovery.

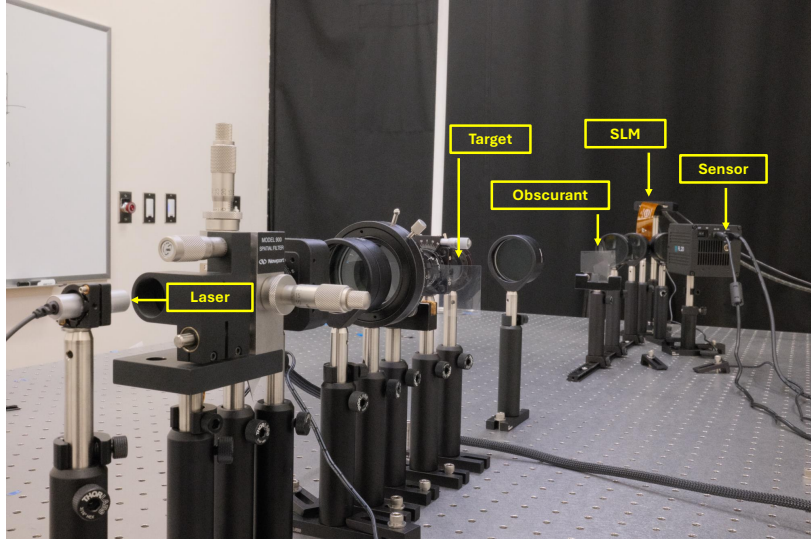


Figure 9: Photo of optical setup. The setup begins with a collimated 520 nm laser that passes through a polarizer and a rotating diffuser. The beam then illuminates the target, a natural scene. The obscurant is positioned at the Fourier plane. A 4f system relays the aberration plane onto the SLM, and the resulting wavefront is imaged onto the camera sensor.

Quantitative results are summarized in Table 3, which reports PSNR and SSIM for each method. Our PSF estimation pipeline achieves performance nearly matching that obtained with the true PSF.

5.2 Experimental Results

Hardware Implementation. Figs. 8 and 9 illustrate our experimental setup. The light source is a collimated 520 nm laser beam that passes through a polarizer and a rotating diffuser to provide spatial incoherence and reduce speckle. This beam illuminates the target, a natural scene. For natural scenes, we use physically printed images to ensure reproducible testing conditions. Lens L1 ($f = 400$ mm) performs a Fourier transform of the target, and the obscurants (nail polish, onion skin, or a 1° diffuser) are placed in the Fourier plane. Lenses L2 and L3 ($f = 100$ mm each) form a 4f system that relays the aberration plane onto the HOLOEYE LETO-3 phase-only SLM, which corrects the distorted wavefront. Lens L4 ($f = 100$ mm) then images the SLM output onto the Tucsen 20 MP FL-20 sensor and yields a 4x reduction. To realize different apertures, we display a checkerboard pattern on the SLM at regions where zero amplitude is desired [28]. This setup adapts flexibly to different targets and magnifications.

To evaluate the generalization ability of our method, we conduct guidestar-free wavefront shaping experiments by imaging through real-world obscurants, including nail polish, onion skin, and 1° diffusers. The optical setup allows us to compare three aperture types—triangular (asymmetric), circular, and rectangular (both symmetric).

Testing images are randomly selected from a held-out subset of the MIT Places2 dataset [52], printed on transparent film, and positioned at the target plane as shown in Figs. 8 and 9. As illustrated in Fig. 10, wavefront correction with the asymmetric triangular aperture is more effective than with the symmetric rectangular and

circular apertures. Importantly, our method provides robust optical correction even in cases when state-of-the-art image deblurring algorithms fail.

For quantitative evaluation, we report PSNR and SSIM for each aperture type in Table 2. We evaluate ten scenes for each obscurant type, with distinct unknown obscurants in every experiment. The results consistently show that the asymmetric triangular aperture yields the highest correction performance.

6 Discussion

In summary, we have introduced a powerful real-time closed-loop AO framework that operates without guidestars, coded measurements, or specialized wavefront sensors. Our system combines deep learning and asymmetric apertures to enable high-quality imaging through severe unknown real-world obscurants. Compared to existing guidestar-free wavefront shaping and image deblurring methods, our approach consistently delivers superior image restoration quality while requiring significantly fewer measurements and far less computation. By helping remove the need for guidestars, this work significantly expands the range of applications in which AO can be applied.

Limitations and Future Work. At present, our system is restricted to correcting spatially invariant isoplanatic optical aberrations, i.e., aberrations within the memory effect region. One could digitally correct anisoplanatic aberrations with our system by imaging patch-by-patch through a scene and stitching together the results. Alternatively, one could optically correct anisoplanatic aberrations with a multi-conjugate extension of our approach—such an extension represents an exciting direction for future work. Likewise, while our guidestar-free aberration technique is computationally lightweight, our current system was not optimized for latency. At present, I/O bottlenecks between the SLM, camera, and computer limit our system’s refresh rate to 1 frame per second (FPS). These

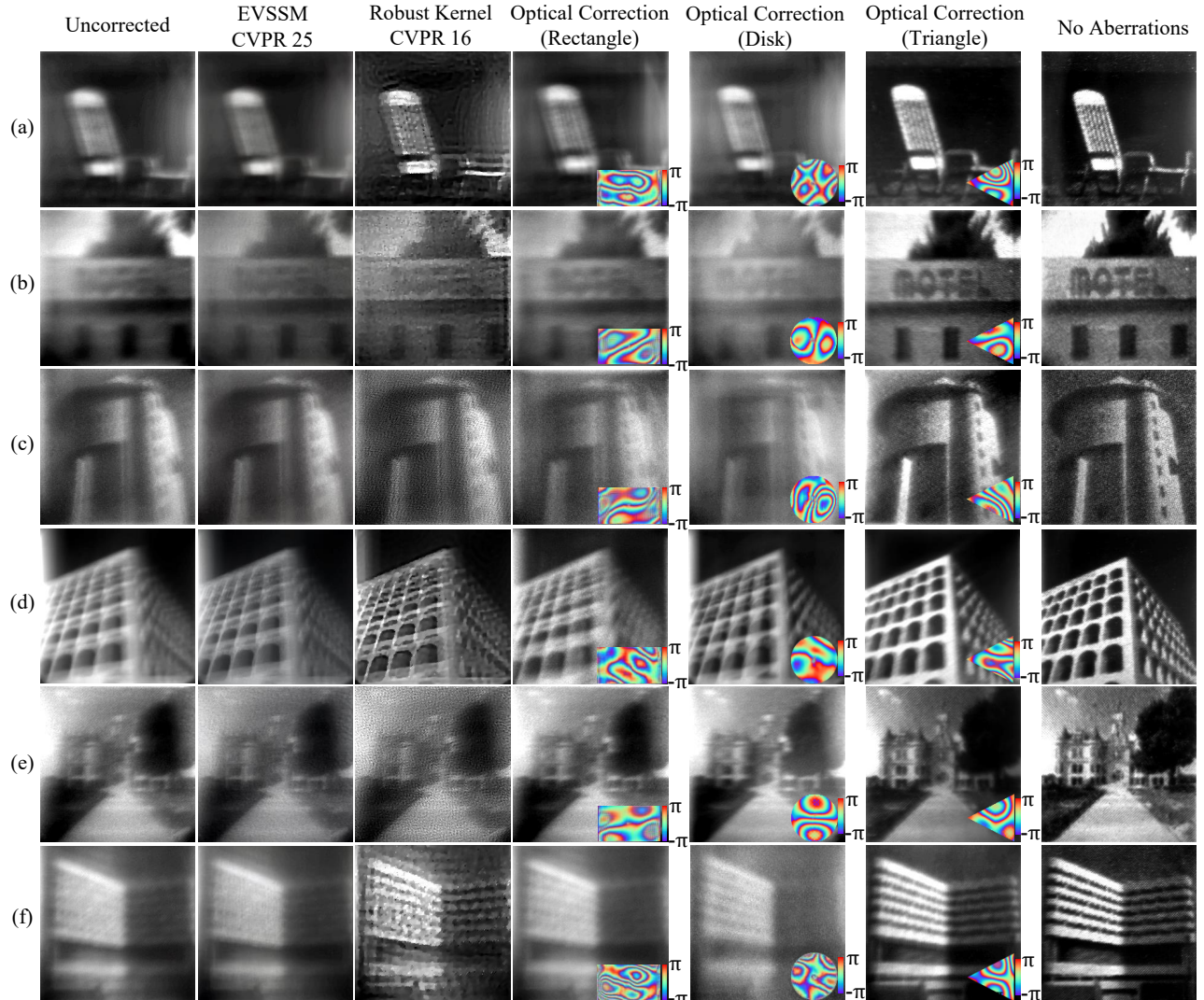


Figure 10: Experimental results for guidestar-free imaging through real-world obscurants. Experimental results demonstrate imaging through different obscurants: (a-b) nail polish, (c-d) onion skin, and (e-f) a 1° diffuser. For each obscurant, columns show the uncorrected image, reconstructions by EVSSM [24] and Robust Kernel al. [32], optical corrections using rectangular, disk, and triangular apertures (with the corresponding estimated phase shown in the lower-right corner), and a no-aberration reference. Rectangular and disk apertures fail to recover fine details, while the triangular aperture leads to substantial improvement in image sharpness. Neither the state-of-the-art deep learning method EVSSM [24] nor the traditional approach of Robust Kernel [32] is able to restore the image, highlighting the benefit of our method.

bottlenecks are not fundamental in nature and, with additional engineering effort, our system could run far faster.

References

- [1] Jeffrey Alido, Joseph Greene, Yujia Xue, Guorong Hu, Yunzhe Li, Mitchell Gilmore, Kevin J Monk, Brett T DiBenedictis, Ian G Davison, and Lei Tian. 2024. Robust single-shot 3D fluorescence imaging in scattering media with a simulator-trained neural network. *Optics Express* 32, 4 (2024), 6241–6257.
- [2] Marina Alterman, Chen Bar, Ioannis Gkioulekas, and Anat Levin. 2021. Imaging with local speckle intensity correlations: theory and practice. *ACM Transactions on Graphics (TOG)* 40, 3 (2021), 1–22.
- [3] Chen Bar, Ioannis Gkioulekas, and Anat Levin. 2020. Rendering near-field speckle statistics in scattering media. *ACM Transactions on Graphics (TOG)* 39, 6 (2020), 1–18.
- [4] Francis Bennet, Celine D’Orgeville, Ian Price, Francois Rigaut, Ian Ritchie, and C Smith. 2015. Adaptive optics for satellite imaging and space debris ranging. In *Proceedings of the Advanced Maui Optical and Space Surveillance Technologies Conference*, Ryan, S., ed, Vol. 1.
- [5] Haoming Cai, Jingxi Chen, Brandon Feng, Weiyun Jiang, Mingyang Xie, Kevin Zhang, Cornelia Fermuller, Yiannis Aloimonos, Ashok Veeraraghavan, and Chris Metzler. 2025. Temporally Consistent Atmospheric Turbulence Mitigation with Neural Representations. *Advances in Neural Information Processing Systems* 37 (2025), 44554–44574.
- [6] JN Cederquist, JR Fienup, CC Wackerman, SR Robinson, and D Kryskowski. 1989. Wave-front phase estimation from Fourier intensity measurements. *Journal of the Optical Society of America A* 6, 7 (1989), 1020–1026.
- [7] Jae Won Cha, Jerome Ballesta, and Peter TC So. 2010. Shack-Hartmann wavefront-sensor-based adaptive optics system for multiphoton microscopy. *Journal of biomedical optics* 15, 4 (2010), 046022–046022.

[8] Stanley H Chan, Nicholas Chimitt, et al. 2023. Computational imaging through atmospheric turbulence. *Foundations and Trends® in Computer Graphics and Vision* 15, 4 (2023), 253–508.

[9] J-C Chanteloup. 2005. Multiple-wave lateral shearing interferometry for wave-front sensing. *Applied optics* 44, 9 (2005), 1559–1571.

[10] Shiqi Chen, Huajun Feng, Dexin Pan, Zhihai Xu, Qi Li, and Yueling Chen. 2021. Optical Aberrations Correction in Postprocessing Using Imaging Simulation. *ACM Trans. Graph.* 40, 5, Article 192 (Sept. 2021), 15 pages. doi:10.1145/3474088

[11] Nicholas Chimitt, Ali Almualem, and Stanley H Chan. 2024. Phase retrieval of a point spread function. In *Unconventional Imaging, Sensing, and Adaptive Optics 2024*. Vol. 13149. SPIE, 220–224.

[12] Nicholas Chimitt, Ali Almualem, Qi Guo, and Stanley H Chan. 2025. Wavefront Estimation From a Single Measurement: Uniqueness and Algorithms. *arXiv preprint arXiv:2504.09395* (2025).

[13] Zhenxuan Fang, Fangfang Wu, Weisheng Dong, Xin Li, Jinjin Wu, and Guangming Shi. 2023. Self-supervised non-uniform kernel estimation with flow-based motion prior for blind image deblurring. In *Proceedings of the IEEE/CVF conference on computer vision and pattern recognition*. 18105–18114.

[14] Brandon Y Feng, Haiyun Guo, Mingyang Xie, Vivek Boominathan, Manoj K Sharma, Ashok Veeraraghavan, and Christopher A Metzler. 2023. NeuWS: Neural wavefront shaping for guidestar-free imaging through static and dynamic scattering media. *Science Advances* 9, 26 (2023), eadg4671.

[15] James R Fienup. 1982. Phase retrieval algorithms: a comparison. *Applied optics* 21, 15 (1982), 2758–2769.

[16] Kshitiz Garg and Shree K Nayar. 2004. Detection and removal of rain from videos. In *Proceedings of the 2004 IEEE Computer Society Conference on Computer Vision and Pattern Recognition, 2004. CVPR 2004*, Vol. 1. IEEE, 1–I.

[17] Robert A Gonsalves. 1982. Phase retrieval and diversity in adaptive optics. *Optical Engineering* 21, 5 (1982), 829–832.

[18] Joseph W Goodman. 2005. *Introduction to Fourier optics*. Roberts and Company publishers.

[19] Yu Guo, Adrian Jarabo, and Shuang Zhao. 2021. Beyond Mie theory: Systematic computation of bulk scattering parameters based on microphysical wave optics. *ACM Transactions on Graphics (TOG)* 40, 6 (2021), 1–12.

[20] David P Haefner. 2018. MTF measurements, identifying bias, and estimating uncertainty. In *Infrared Imaging Systems: Design, Analysis, Modeling, and Testing XXIX*, Vol. 10625. SPIE, 54–68.

[21] Omri Haim, Jeremy Boger-Lombard, and Ori Katz. 2025. Image-guided computational holographic wavefront shaping. *Nature Photonics* 19, 1 (2025), 44–53.

[22] Qianyue He, Dongyu Du, Haitian Jiang, and Xin Jin. 2024. DARTS: Diffusion Approximated Residual Time Sampling for Time-of-flight Rendering in Homogeneous Scattering Media. *ACM Trans. Graph.* 43, 6, Article 240 (Nov. 2024), 14 pages. doi:10.1145/3687930

[23] Weiyun Jiang, Vivek Boominathan, and Ashok Veeraraghavan. 2023. Nert: Implicit neural representations for unsupervised atmospheric turbulence mitigation. In *Proceedings of the IEEE/CVF Conference on Computer Vision and Pattern Recognition Workshops*. 4236–4243.

[24] Lingshun Kong, Jiangxin Dong, Jinhu Tang, Ming-Hsuan Yang, and Jinshan Pan. 2025. Efficient visual state space model for image deblurring. In *Proceedings of the Computer Vision and Pattern Recognition Conference*. 12710–12719.

[25] Nektarios Koukourakis, Bob Fregin, Jörg König, Lars Büttner, and Jürgen W Czarske. 2016. Wavefront shaping for imaging-based flow velocity measurements through distortions using a Fresnel guide star. *Optics Express* 24, 19 (2016), 22074–22087.

[26] Shi Mao, Yogeshwar Mishra, and Wolfgang Heidrich. 2025. Fovea Stacking: Imaging with Dynamic Localized Aberration Correction. *arXiv preprint arXiv:2506.00716* (2025).

[27] Frantz Martinache. 2013. The asymmetric pupil Fourier wavefront sensor. *Publications of the Astronomical Society of the Pacific* 125, 926 (2013), 422.

[28] Omel Mendoza-Yero, Gladys Mínguez-Vega, and Jesús Lancis. 2014. Encoding complex fields by using a phase-only optical element. *Optics letters* 39, 7 (2014), 1740–1743.

[29] Laurent M Mugnier, Amandine Blanc, and Jérôme Idier. 2006. Phase diversity: a technique for wave-front sensing and for diffraction-limited imaging. *Advances in Imaging and Electron Physics* 141 (2006), 1–76.

[30] Vasilis Ntziachristos. 2010. Going deeper than microscopy: the optical imaging frontier in biology. *Nature methods* 7, 8 (2010), 603–614.

[31] Jaime Ortega-Arroyo and Philipp Kukura. 2012. Interferometric scattering microscopy (iSCAT): new frontiers in ultrafast and ultrasensitive optical microscopy. *Physical Chemistry Chemical Physics* 14, 45 (2012), 15625–15636.

[32] Jinshan Pan, Zhouchen Lin, Zhixun Su, and Ming-Hsuan Yang. 2016. Robust kernel estimation with outliers handling for image deblurring. In *Proceedings of the IEEE Conference on Computer Vision and Pattern Recognition*. 2800–2808.

[33] Richard G Paxman, Timothy J Schulz, and James R Fienup. 1992. Joint estimation of object and aberrations by using phase diversity. *Journal of the Optical Society of America A* 9, 7 (1992), 1072–1085.

[34] Michael Pircher and Robert J Zawadzki. 2017. Review of adaptive optics OCT (AO-OCT): principles and applications for retinal imaging. *Biomedical optics express* 8, 5 (2017), 2536–2562.

[35] Ben C Platt and Roland Shack. 2001. History and principles of Shack-Hartmann wavefront sensing. S573–S577 pages.

[36] Lisa A Poyneer. 2003. Scene-based Shack-Hartmann wave-front sensing: analysis and simulation. *Applied Optics* 42, 29 (2003), 5807–5815.

[37] Changhui Rao, Libo Zhong, Youming Guo, Min Li, Lanqiang Zhang, and Kai Wei. 2024. Astronomical adaptive optics: a review. *PhotonIX* 5, 1 (2024), 16.

[38] François Roddier. 1999. Adaptive optics in astronomy. (1999).

[39] Michael C Roggemann and Byron M Welsh. 2018. *Imaging through turbulence*. CRC press.

[40] José Sasián. 2012. *Introduction to aberrations in optical imaging systems*. Cambridge University Press.

[41] Guy Satat, Matthew Tancik, and Ramesh Raskar. 2018. Towards photography through realistic fog. In *2018 IEEE International Conference on Computational Photography (ICCP)*. IEEE, 1–10.

[42] Qilin Sun, Congli Wang, Fu Qiang, Dun Xiong, and Heidrich Wolfgang. 2021. End-to-end complex lens design with differentiable ray tracing. *ACM Trans. Graph.* 40, 4 (2021), 1–13.

[43] Lei Tian and Laura Waller. 2015. Quantitative differential phase contrast imaging in an LED array microscope. *Optics express* 23, 9 (2015), 11394–11403.

[44] Robert K Tyson. 1996. Adaptive optics and ground-to-space laser communications. *Applied optics* 35, 19 (1996), 3640–3646.

[45] Robert K Tyson. 2002. Bit-error rate for free-space adaptive optics laser communications. *Journal of the Optical Society of America A* 19, 4 (2002), 753–758.

[46] Gregory E Wood, Michael C Roggemann, and Byron M Welsh. 1997. Estimation of satellite orientation from space surveillance imagery measured with an adaptive optics telescope. In *Propagation and Imaging through the Atmosphere*, Vol. 3125. SPIE, 226–233.

[47] Jianmin Wu, Yuduo Guo, Chao Deng, Anke Zhang, Hui Qiao, Zhi Lu, Jiachen Xie, Lu Fang, and Qionghai Dai. 2022. An integrated imaging sensor for aberration-corrected 3D photography. *Nature* 612, 7938 (2022), 62–71.

[48] Mingyang Xie, Haiyun Guo, Brandon Y Feng, Lingbo Jin, Ashok Veeraraghavan, and Christopher A Metzler. 2024. Wavemo: Learning wavefront modulations to see through scattering. In *Proceedings of the IEEE/CVF Conference on Computer Vision and Pattern Recognition*. 25276–25285.

[49] Tomer Yemini and Ori Katz. 2021. Guidestar-free image-guided wavefront shaping. *Science advances* 7, 21 (2021), eabf5364.

[50] Gavin Young and Philipp Kukura. 2019. Interferometric scattering microscopy. *Annual review of physical chemistry* 70, 1 (2019), 301–322.

[51] Qinrong Zhang, Qi Hu, Caroline Berlage, Peter Kner, Benjamin Judkewitz, Martin Booth, and Na Ji. 2023. Adaptive optics for optical microscopy. *Biomedical Optics Express* 14, 4 (2023), 1732–1756.

[52] Bolei Zhou, Agata Lapedriza, Aditya Khosla, Aude Oliva, and Antonio Torralba. 2017. Places: A 10 million image database for scene recognition. *IEEE transactions on pattern analysis and machine intelligence* 40, 6 (2017), 1452–1464.

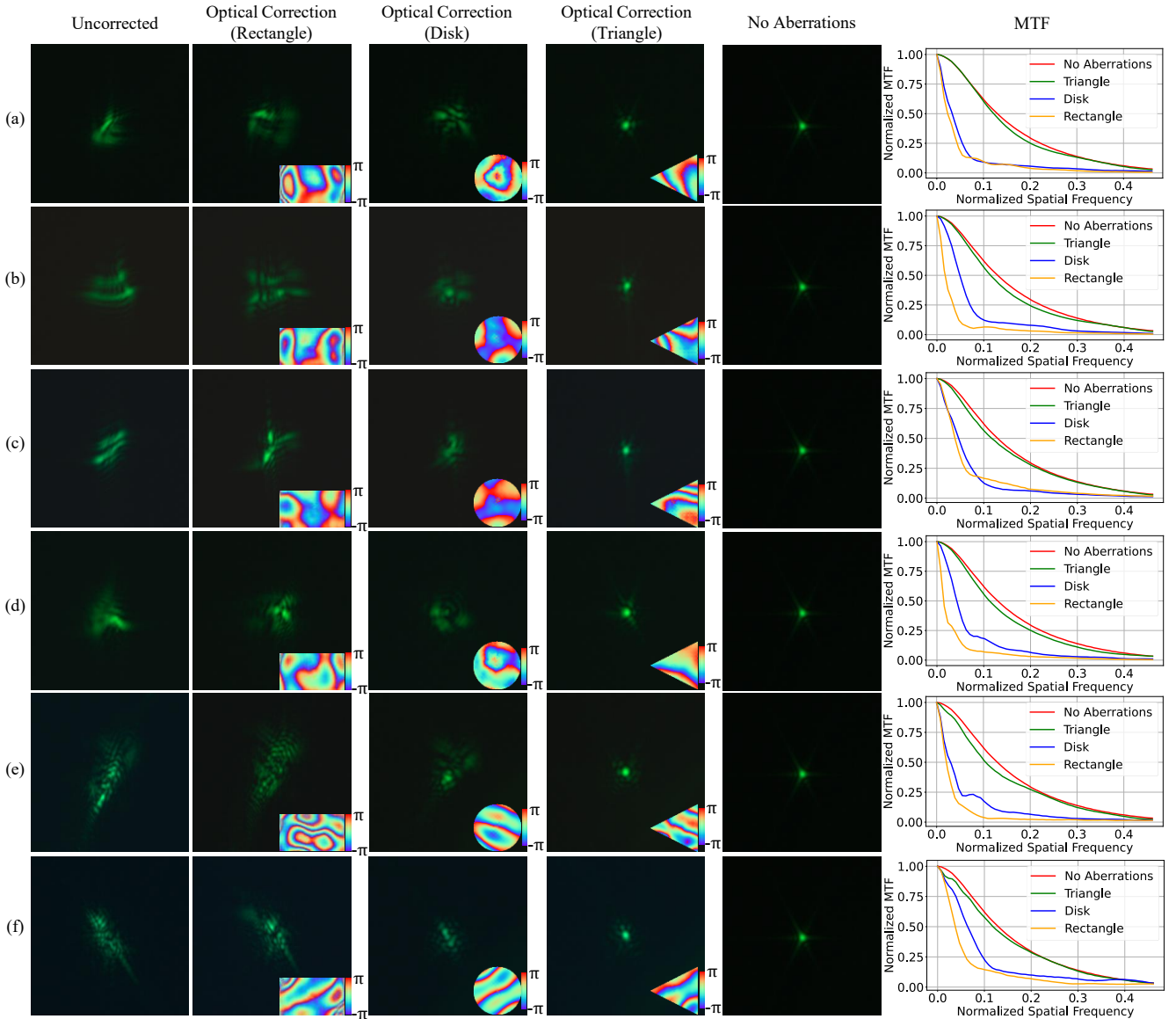


Figure 11: Guidestar-based experimental validation of phase U-Net generalization. Experimental pinhole imaging through (a–b) nail polish, (c–d) onion skin, and (e–f) a 1° diffuser. Columns show the uncorrected image, corrected results using rectangular, disk, and triangular apertures (with estimated phase at lower right), the no-aberration reference, and MTF plots. Although trained only on Zernike-based aberrations, the phase U-Net corrects real aberrations effectively.

A Guidestar-Based Real Experiments

While our primary contribution is a guidestar-free correction pipeline, we also provide supplementary experiments to demonstrate that our method is effective when a guidestar is available. In these experiments, instead of using our proposed PSF U-Net to estimate the PSF from a blurred measurement, we directly use the PSF captured with a pinhole guidestar and feed it to the phase U-Net for phase recovery. This setup bypasses the PSF estimation step and is designed to directly validate the performance of our phase U-Net when the

ground truth PSF is available. These experiments are analogues to those performed concurrently in [12].

Beyond qualitative comparisons of PSF corrections in Fig. 11, we quantitatively assess performance by analyzing the modulation transfer function (MTF) for all three aperture shapes. The MTF characterizes the system’s ability to preserve image contrast across spatial frequencies and is a standard metric for evaluating imaging resolution and quality [20, 42, 43]. The results confirm that our asymmetric triangular aperture achieves a higher MTF compared to conventional symmetric designs, further validating its effectiveness in wavefront correction.

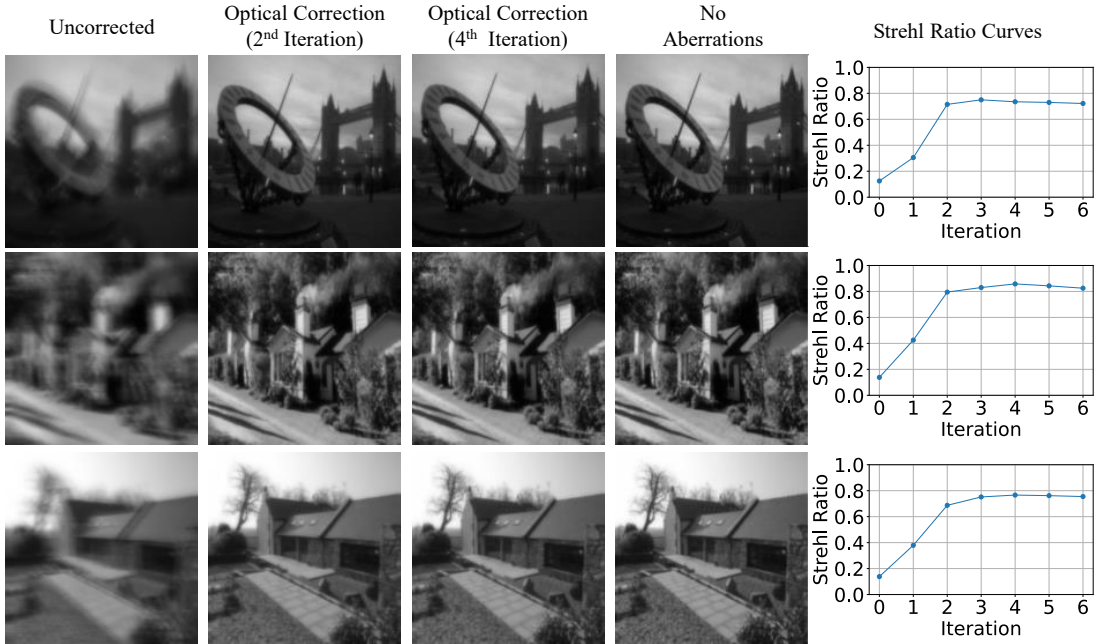


Figure 12: Strehl ratio across iterations. Most optical aberrations are corrected within the first two iterations, with subsequent iterations providing smaller improvements. The Strehl ratio—defined as the peak intensity of the corrected wavefront normalized by the peak intensity of an ideal diffraction-limited system—quantifies the effectiveness of aberration correction. Higher Strehl ratios correspond to improved image quality. This motivates us to use four iterations throughout our experiments.

Table 4: Quantitative evaluation of PSNR / SSIM on real-world experiments under different obscurants and apertures. We test 10 scenes for each aberration type (nail polish, onion skin, and diffusers). Obscurants are distinct in every experiment. Three apertures are evaluated and the results indicate that the triangular aperture exhibits superior performance.

Apertures	Obscurants		
	Nail Polish	Onion Skin	Diffusers
Rectangle	14.98 / 0.5290	15.65 / 0.4849	15.59 / 0.4852
Disk	15.36 / 0.5543	15.13 / 0.4572	14.99 / 0.4791
Triangle	25.51 / 0.7286	25.82 / 0.7885	24.67 / 0.7093

It is important to note that both the PSF and phase used for training the phase U-Net are generated from Zernike aberration profiles. Therefore, these real-world experiments further demonstrate that our phase U-Net generalizes well beyond Zernike-based synthetic data and performs robustly under real, complex aberrations introduced by real-life obscurants.

B Reproducibility

To facilitate reproducibility, we will release our code in two forms. The first version will include all data generation scripts, allowing users to train the model on their own data. The second version will

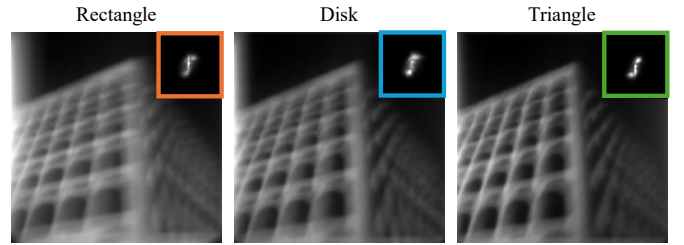


Figure 13: PSF U-Nets perform equally well across different apertures. The performance of PSF U-Net remains consistent for rectangular, circular, and triangular apertures. This indicates that the improved optical correction observed with asymmetric triangular apertures depends solely on whether the Phase U-Net can resolve ambiguities and retrieve the unique phase.

provide a pretrained model, which can be used directly for baseline comparisons.

C Quantitative Evaluation of PSNR and SSIM on Real-World Experiments Under Different Obscurants and Apertures

Table 4 demonstrates that the asymmetric triangular aperture outperforms the other two symmetric apertures across all three obscurants, highlighting its superior capability for unambiguous wavefront corrections.

D Aperture Shape Does Not Affect PSF Estimation

To assess the influence of aperture shape on PSF U-Net performance, we evaluate its accuracy with triangular, rectangular, and circular apertures using the same obscurant (Fig. 13). The consistent results across different aperture shapes demonstrate that PSF U-Net provides reliable PSF estimation regardless of aperture geometry, and does not limit the overall effectiveness of optical correction.

E Strehl Ratio-Based Iteration Selection

To evaluate the convergence of our aberration correction pipeline, we monitor the Strehl ratio across iterations. As shown in Fig. 12, the Strehl ratio improves rapidly in the first two iterations, indicating that most aberrations are corrected early in the process. Additional iterations provide smaller improvements, gradually reducing residual errors. Based on this analysis, we fix the number of iterations to four throughout our experiments to ensure both performance and efficiency.